Ab-initio and Monte Carlo study of Fe-based two-dimensional magnets at borophene supported by Ag(111) surface

Božidar N. Šoškić,[1] Srdjan Stavrić,[2,3] and Željko Šljivančanin[3,*]

[1]*Faculty of Natural Sciences and Mathematics, University of Montenegro, Džordža Vašingtona bb, 81000 Podgorica, Montenegro*

[2]*Physics Department, University of Trieste, via A. Valerio 2, Trieste 34127, Italy*

[3]*Vinča Institute of Nuclear Sciences, National Institute of the Republic of Serbia, University of Belgrade, P. O. Box 522, RS-11001 Belgrade, Serbia*

(Received 24 March 2021; revised 17 June 2021; accepted 22 June 2021; published 1 July 2021)

Two-dimensional (2D) magnetic crystals are ideal platforms for the employment of simple physical models in the exploration of magnetism in a 2D limit. Instead of examining 2D van der Waals materials, the focus of our study is on adatoms that carry intrinsic magnetic moments and are assembled into 2D arrays at a suitable surface. We applied density functional theory (DFT) to investigate Fe nanostructures formed on a borophene sheet deposited at Ag(111) surface and identified stable Fe-based 2D magnets formed either on top of the borophene or at the interface between the borophene and Ag(111) surface. The structures are composed of close-packed Fe wires, featuring ferromagnetism within the chain and the interchain antiferromagnetic coupling. Exchange- and single-ion anisotropy constants extracted from DFT calculations are used to describe these systems with the classical Ising and Heisenberg models. The corresponding Monte Carlo simulations revealed finite temperature magnetic ordering, with the estimates of critical temperatures of 105 and 30 K derived from the anisotropic Heisenberg model, for the Fe-based magnets grown above and under borophene, respectively.

DOI: 10.1103/PhysRevMaterials.5.074001

I. INTRODUCTION

The isolation of a single graphene layer in 2004 [1], followed by the demonstration of numerous fascinating physical and chemical properties [2,3], triggered the research focused on two-dimensional (2*D*) crystals and produced an ample amount of new 2*D* materials with diverse structural and electronic properties [4–7]. Nonetheless, in the landscape of van der Waals materials produced by a simple mechanical exfoliation, only a few exhibit nontrivial magnetic properties [8]. In addition, for being among the most promising candidates for possible applications in spintronics [9], these materials are precious tools for testing the fundamental physical models of magnetism in a 2*D* limit. According to recent studies, a monolayer of ferromagnetic isolator CrI_3 preserves magnetic order up to 45 K [10], a $FePS_3$ monolayer was reported to display an Ising-type antiferromagnetic ordering [11], and $Cr_2Ge_2Te_6$ was described as a nearly ideal two-dimensional Heisenberg ferromagnet [12].

In graphene, hexagonal boron nitride (h-BN), and other most common nonmagnetic 2*D* materials, fabrication of structural defects and/or doping with magnetic atoms are the simplest approaches to induce magnetism. Density functional theory (DFT) calculations indicated the emergence of spin-polarized states at the monovacancies of graphene [13] and later experiments demonstrated the paramagnetic nature of defected graphene sheet [14]. Nonzero magnetic moments were also reported at C atoms buried in other defects of honeycomb lattice [15], graphene edges [16,17] or graphene functionalized with hydrogen [18,19] or fluorine [20]. Additionally, the doping with metal atoms was used to induce magnetism in transition metal dichalcogenides [21,22] and to enrich their functionalities. However, when adsorbed at graphene or h-BN, transition metal adatoms tend to cluster [23], which indicates efforts to control the size and electronic properties of deposited metal nanostructures. On the other hand, the same adatoms attached to the point defects of graphene or h-BN are structurally very stable and do not agglomerate [24], since monoatomic defects act as trapping centers that prevent diffusion of adatoms and suppress their aggregation into bigger structures. The metal atoms embedded into point defects might carry out nonzero magnetic moments, yet these defects are randomly distributed across graphene or h-BN which makes the long-range ordering of atomic magnetic moments highly unlikely [14].

Recently Feng *et al.* synthesized a sheet of 2*D* boron, borophene (B-2D), using Ag(111) surface as a substrate [25]. The borophene lattice is a triangular structure composed of the six-coordinated B atoms mixed with five- and four-coordinated atoms around the holes, arranged into perfect arrays. Using the same substrate Mannix *et al.* generated other borophene polymorphs and studied their structural and electronic properties [26]. These experiments confirmed the existence of stable B-2D crystal predicted by first-principles calculations [27], while further research resulted in the atomistic description of the growth mechanism of borophene on Ag(111) [28]. Moreover, the borophene has also been grown at Al(111) [29], Au(111) [30], Cu(111) [31], and Ni(111) surfaces [27]. DFT calculations also predicted borophene with

*zeljko@vinca.rs

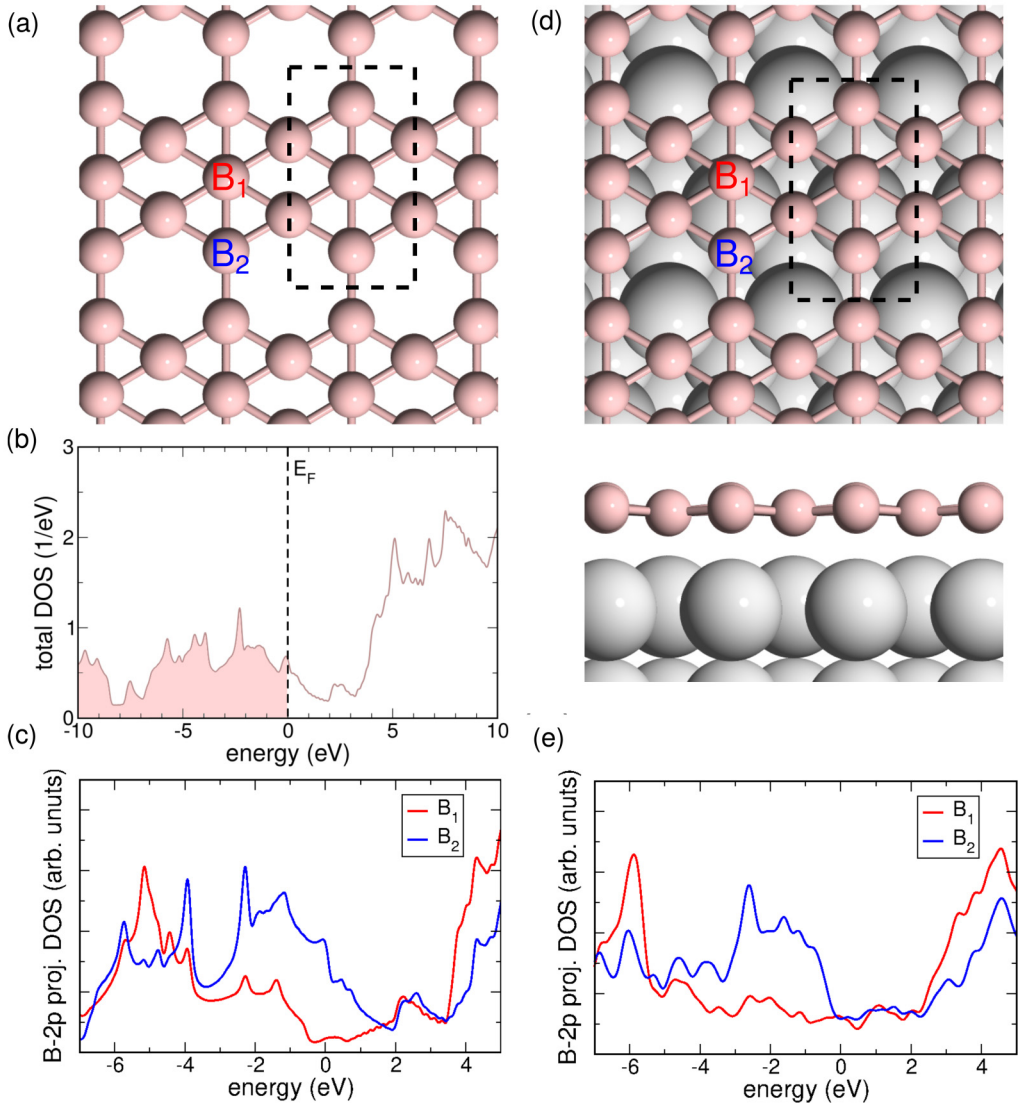

FIG. 1. (a) Top view of free-standing borophene sheet; the corresponding (b) total DOS and (c) DOS projected on $2p$ orbitals of six- and four-coordinated B atoms, labeled as B_1 and B_2, respectively; (d) top and side view of the borophene sheet on Ag(111); (e) the corresponding DOS projected on $2p$ orbitals of six- and four-coordinated B atoms. Boron and silver atoms are presented by small ochre and big gray spheres, respectively.

larger holes [32], and later theoretical studies suggested superconductivity in borophene [33]. Overviews on the recent results were presented in Refs. [34,35] .

In the present manuscript we applied DFT to explore the prospects of using borophene deposited on silver (B-2D/Ag(111)) as a template to grow well-ordered Fe nanostructures. At variance with randomly generated point defects in graphene, the holes in borophene are well-ordered and closely packed, hence they might stabilize different kinds of regular magnetic nanostructures when decorated with Fe adatoms. Exploiting this particular property of borophene mesh, we identified the most stable nanostructures of Fe adatoms, studied their spin magnetism, and inspected their ability to sustain the long-range magnetic order.

The manuscript is organized as follows: Section II contains the description of the computational methodology applied in this work; in Sec. III are presented the results on structural and magnetic properties of Fe atoms at B-2D/Ag(111) found combining DFT, simple models and Monte Carlo simulations. Finally, the main findings are summarized in Sec. IV.

II. COMPUTATIONAL DETAILS

DFT calculations were carried out with QUANTUM ESPRESSO package [36,37], based on pseudopotentials and the plane waves. The wave functions and the electron density were expanded in plane waves with cutoff energies of 45 and 300 Ry, respectively. The exchange and correlation effects in the electron gas were taken into account by means of Perdew-Burke-Ernzerhof parametrization form within generalized gradient approximation [38], and the electronic states were occupied employing the Methfessel-Paxton smearing with the smearing parameter of 0.03 eV. The free-standing B-2D as well as B-2D on Ag(111) were modeled within the (1×1) surface cell depicted in Fig. 1(a), periodically repeated in the plane of the $2D$ crystal. To represent Ag(111) surface

we used a three-layer slab, with at least 20 Å of vacuum. All B, as well as all Ag atoms except those from the bottom layer were allowed to relax until the forces on atoms are less than 0.02 eV/Å. The relaxation was performed employing the Broyden-Fletcher-Goldfarb-Shanno (BFGS) algorithm [39]. The atoms from bottom Ag(111) layer were fixed in their bulk positions. The surface Brillouin-zone (BZ) of the (1×1) surface cell was sampled with 256 special **k** points [40]. The calculations of Fe monomers, dimers, trimers, and infinite Fe chains at free-standing or Ag(111)-supported B-2D were carried out using (4×2) surface cell, and the BZ sampling was adjusted to match the **k**-point density to the one used in the calculations with the (1×1) cell. Magnetic anisotropy energy (MAE) of Fe nanostructures, needed for the derivation of single-ion anisotropy constants, were calculated with WIEN2K code [41]. In particular, MAE is obtained with force theorem approach [42] from calculations with spin-orbit coupling included as a difference in band energies for two magnetization directions—one pointing along the direction perpendicular to the Ag(111) surface (easy axis) and another parallel to the Fe chains (hard axis). We used the Atomic Simulation Environment package to setup and display studied structures [43,44] and XCrysden [45] for contour plots of induced charge density.

Monte Carlo simulations were carried out on a square lattices with 100×100 sites, applying periodic boundary conditions, and the Metropolis algorithm to update spins. The initial, random spin configurations were equilibrated performing 100 000 steps per lattice site, and then additional 100 000 steps per site were used to calculate the average magnetization at a given temperature. To improve the accuracy of the simulations, this procedure was repeated 20 times and the mean values were reported as the final results.

III. RESULTS AND DISCUSSION

A. Pristine borophene (B-2D)

The borophene (B-2D), depicted in Fig. 1(a), represents a sheet of B atoms, arranged in a triangular lattice with a regular, close-packed hexagonal holes (HH) due to missing B atoms. Depending on the holes arrangement, there are different B-2D phases. In this work we studied the β_{12} [25,46] phase which, according to recent scanning tunneling microscopy (STM) measurements and DFT calculations, can be deposited on Ag(111) in several different manners [25,47] with similar adhesion energies. We focus on the S3 phase presented in Ref. [47] and here depicted in Fig. 1(d), since it provides a suitable framework to grow well-ordered Fe structures. DFT-calculated lattice parameters of the S3 phase, $a = 2.94$ and $b = 5.09$ Å, agree well with the findings from the experimental STM imaging as well as with previous DFT calculations [47,48]. The total density of states (DOS) plot [Fig. 1(b)] demonstrates the metallic character of the sheet. The coordination number of B atoms varies in the range from four and six, which gives rise to the difference in the local electronic properties of the sheet [Fig. 1(c)], with noticeable higher DOS near the Fermi level (E_F) originating from the $2p$ states of the B_2 as compared to those of the B_1 atoms.

Theoretically predicted B-2D has been synthesized only recently [25], using Ag(111) surface as a support. In our model of the B-2D at Ag(111) the arrays of close-packed HH are oriented along the [110] direction of the Ag(111). Since the a lattice parameter of the B-2D matches nearly perfectly with the distance between neighboring Ag atoms, the S3 phase preserves translational symmetry of the underlined metal lattice along the [110] direction. Hence, the B-2D/Ag(111) can be modeled using a small surface unit cell, depicted in Fig. 1(d). DFT calculations reveal a modest interaction between the B-2D and the Ag(111), with the binding energy of 0.12 eV per B atom. The plots of the local electronic properties of the B atoms presented in Fig. 1(e) indicate a substantial charge transfer from Ag(111) substrate to the borophene. The B_2-$2p$ states from the peak near E_F, partially occupied in the free-standing sheet, are shifted below the Fermi level upon borophene adsorption on Ag(111).

B. Fe nanostructures at B-2D/Ag(111)

The differences in the local electronic properties of B atoms, caused by different coordination, are usually directly correlated with their reactivity. When considering the same chemical element, the low-coordinated atoms are expected to bind adsorbates stronger than the atoms with higher coordination. Binding energies obtained from our DFT study of Fe adatoms on free standing or Ag(111)-supported B-2D follow this common trend. The adsorption geometries of Fe atom at B-2D/Ag(111) are depicted in Fig. 2(a) with the corresponding binding energies presented in Fig. 2(b) and listed in Table I. For comparison, in Table I we also provided Fe atom binding energies at the free-standing B-2D, in the adsorption sites equivalent to those of the Ag(111) supported sheet.

The HH sites of B-2D/Ag(111) are by far the most favorable ones, with the binding energies of 3.70 and 3.32 eV for Fe atoms under or above B-2D, respectively. These two adsorption geometries, labeled as I and II, are depicted in Figs. 2(c) and 2(d). We also inspected the diffusion of the Fe atom through the HH, from the site II to the site I, and found that this process is accompanied with the energy barrier of 1.0 eV. Although the binding under the borophene is favored by thermodynamics, if the surface temperature or kinetic energy of deposited atoms is not sufficiently high, the Fe adatom will remain above the borophene surface, trapped in the adsorption site II. The Fe binding energy of 2.98 eV under the sheet in the adsorption geometry III [Fig. 2(a)] is weaker than those under or above the HH, yet it is still significantly stronger than binding to any other site above the sheet (adsorption geometries IV-VII). The binding energies of all seven adsorption sites marked in Fig. 2 are presented in Table I, together with the Fe magnetic moments. For the sake of completeness we included the results for the corresponding adsorption sites on the free-standing borophene. The much stronger binding of Fe atoms on the free-standing sheet when compared to the one supported by Ag(111) is in accordance with the expected decline in the reactivity of the borophene upon the interaction with the Ag(111) surface.

The study of two or more Fe atoms coadsorbed at the B-2D/Ag(111) clearly demonstrates the tendency of adatoms to form dimers. The most stable adsorption geometry of two Fe atoms above the sheet is depicted in Fig. 3(a). The

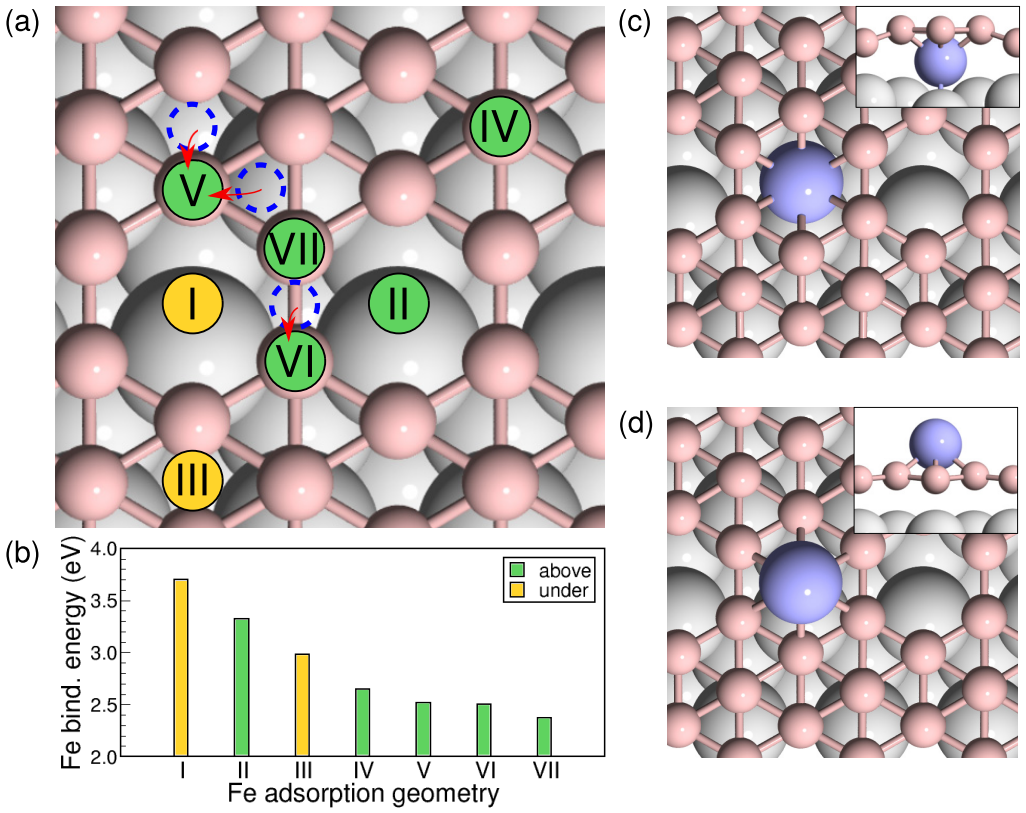

FIG. 2. (a) Fe adsorption sites and (b) the corresponding binding energies at the B-2D/Ag(111). The yellow and green circles represent adsorption sites under and above the borophene, respectively. Unstable adsorption sites are presented by open blue dotted circles and the red arrows are pointed towards the nearest stable adsorption geometries; (c) top and (d) side (inset) views of the most favorable adsorption geometries, labeled as I and II in the panel (a). Fe atoms are depicted as iceblue spheres, and for boron and silver atoms the same color scheme as in Fig. 1 is used.

TABLE I. The binding energies and the magnetic moments per Fe atom, calculated for the adsorption geometries depicted in Fig. 2(a), dimers, trimers, and infinite chains in Fig. 3. For all nanostructures we compared adsorption geometries where Fe atoms were adsorbed above (A) and under (U) borophene sheet at Ag(111).

	Free-standing borophene		B-2D/Ag(111)	
Configuration	Binding energy (eV/atom)	Magnetic moment (μ_B/atom)	Binding energy (eV/atom)	Magnetic moment (μ_B/atom)
I [Fig. 2(a)]	–	–	3.70	2.27
II [Fig. 2(a)]	4.57	1.01	3.32	2.92
III [Fig. 2(a)]	–	–	2.98	1.52
IV [Fig. 2(a)]	2.84	2.18	2.65	3.11
V [Fig. 2(a)]	–	–	2.52	2.81
VI [Fig. 2(a)]	–	–	2.50	2.74
VII [Fig. 2(a)]	–	–	2.37	2.71
Fe_2-A [Fig. 3(a)]	4.85	1.07	3.52	3.01
Fe_2-U [Fig. 3(b)]	–	–	4.21	2.80
Fe_3-A [Fig. 3(c)]	4.78	1.24	3.72	2.29
Fe_3-U [Fig. 3(d)]	–	–	4.33	2.04
Fe_{chain}-A [Fig. 3(e)]	4.88	1.04	3.99	2.07
Fe_{chain}-U [Fig. 3(f)]	–	–	4.34	1.36

corresponding binding energy of 3.52 eV/atom is 0.2 eV/atom higher as compared to the case of a single atom in the site II. The distance between Fe atoms of 2.48 Å is noticeably larger than 2.01 Å, found for the gas-phase Fe_2 [49], but considerably smaller than 2.93 Å, corresponding to the separation between the holes in B-2D at Ag(111). The calculated Fe_2 bond length represents a compromise between the competing effects of the holes' high reactivity, acting in favor of the dimer stretching, and a strong Fe-Fe interaction, giving rise to its contraction. The dimer adsorbed under the borophene [Fig. 3(b)] is considerably more stable than the Fe_2 above the B-2D sheet, with the binding energy of 4.21 eV/atom. The corresponding bond length of 2.40 Å reflects further dimer contraction due to the interaction with Ag(111) surface. The potential energy landscape of the metal surface is flatter than the one of B-2D, and thus the preference for Fe binding at specific adsorption sites is not that pronounced as at borophene. Similar binding trends occur for Fe trimers; the Fe_3 above the borophene [Fig. 3(c)] binds by 3.72 eV/atom, significantly weaker than for the Fe_3 inserted between borophene and Ag(111) [Fig. 3(d)] when the binding energy increases to 4.33 eV/atom. The adsorption energies of Fe atoms from an infinite chain [Fig. 3(e)] show that an elongation of the linear nanostructures further stabilizes Fe adatoms. The chain under the borophene [Fig. 3(f)], like the other Fe nanostructures, are more

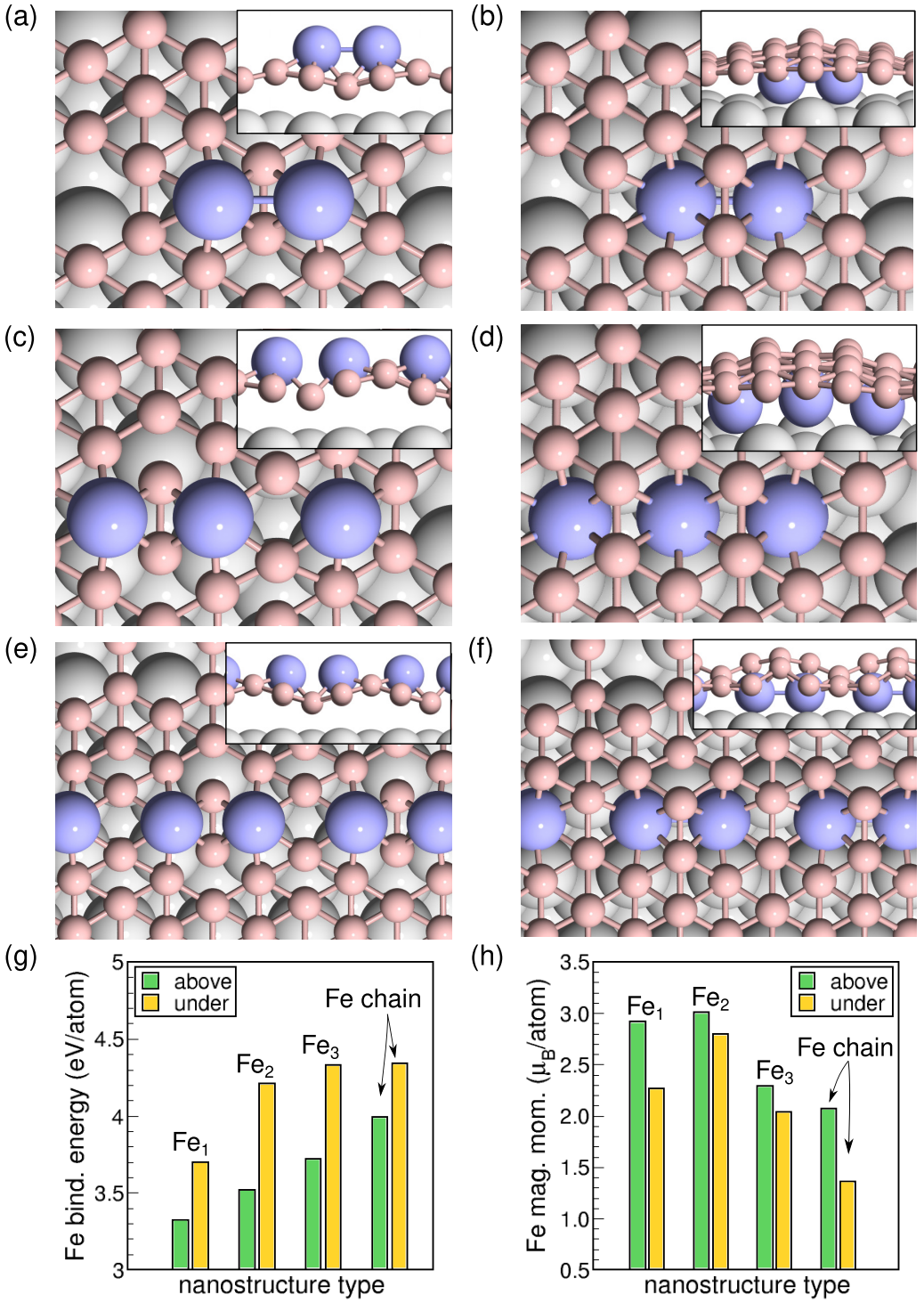

FIG. 3. Top and side (inset) views of Fe (a) dimer, (c) trimer, and (e) an infinite Fe chain above (A) or (b), (d), and (f) under (U) the holes of borophene sheet at Ag(111) surface, respectively; the corresponding (g) adsorption energies, and (h) magnetic moments per Fe atom. The color scheme of atoms is the same as in Fig. 2.

stable than its counterpart above the borophene sheet. All calculated adsorption energies and average magnetic moments of Fe atoms are compared in Figs. 3(g) and 3(h) and listed in Table I.

The Fe adsorption structures in Figs. 2 and 3 are magnetic, with the spin magnetic moment per Fe atom in range from 1.36 μ_B in the chain in Fig. 3(f), to 3.01 μ_B per atom, in the dimer in Fig. 3(a). The magnetic moments at the atoms adsorbed below the sheet, near the Ag(111), are considerably smaller than those of the Fe adatoms on top of the borophene. This is in line with the expectation that stronger binding enhances delocalization of Fe 3*d* states and thus reduces the exchange splitting of their spin-majority and spin-minority states. The Fe adatoms considerably enhance the buckling of

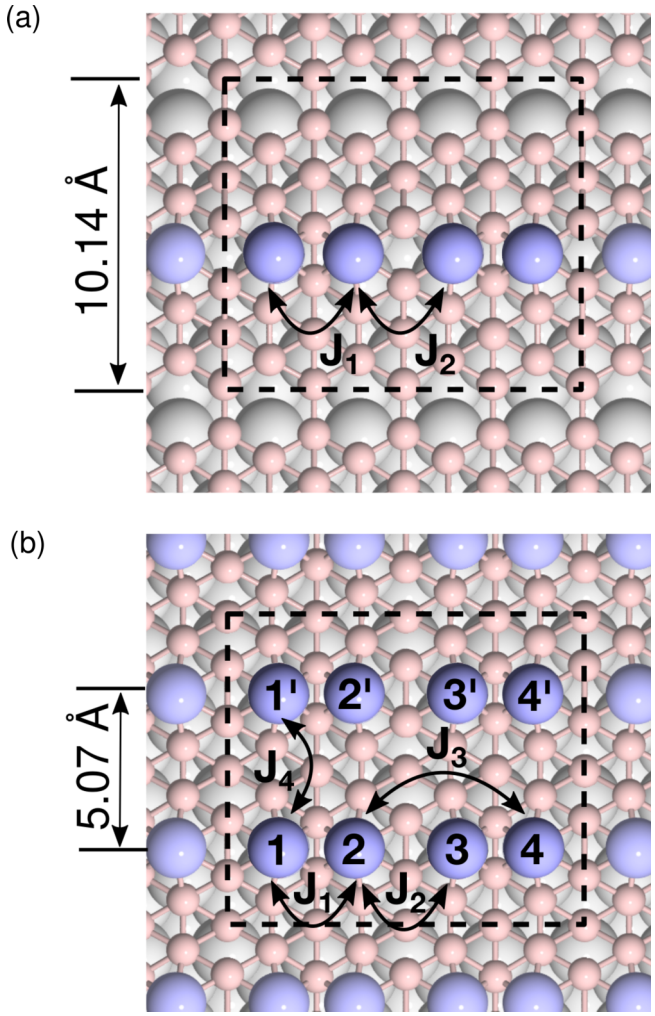

FIG. 4. Top views of the (a) well-separated and (b) closely packed Fe chains on B-2D/Ag(111). The 4 × 2 surface unit cell used in the calculations is marked by a black rectangle. The enumeration of Fe atoms corresponds to Eqs. (1) and (2), and black double arrowed lines indicate the coupling constants between Fe atoms. The color scheme of atoms is the same as in Fig. 2.

the B-2D sheet, from 0.1 Å, calculated for pristine borophene at Ag(111), to the value of 1.37 Å for the Fe trimer at B-2D/Ag(111).

1. Fe wires and Fe-based 2D magnets at B-2D/Ag(111)

Now we focus on the properties of infinite Fe monoatomic wires grown above or under B-2D supported by Ag(111). Using the 4 × 2 surface unit cell (Fig. 4) we studied Fe chains separated by 10.14 Å, considered in this work as noninteracting [Fig. 4(a)], as well as the structures of closely packed Fe wires, where the interchain distance was halved [Fig. 4(b)]. The closer inspection of the structural properties of isolated Fe wires indicate their strong dimerization [Fig. 6(a)], with the distances between the nearest neighbors taking the values of 2.60 to 3.26 Å for the chain above B-2D and from 2.50 to 3.36 Å when Fe chain was inserted between the B-2D and Ag(111). The borophene buckling for the chain is very similar as for the trimer above and under the sheet, respectively. The induced

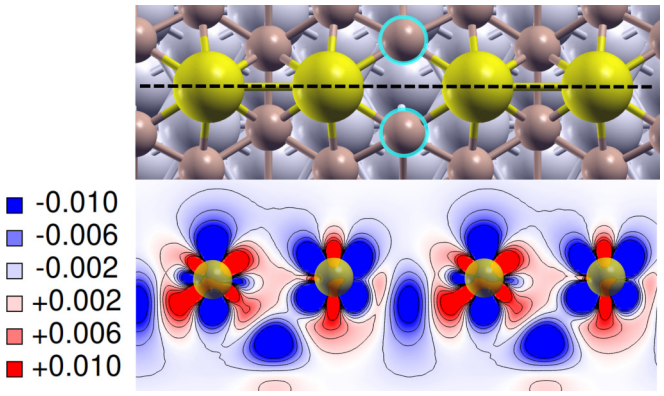

FIG. 5. Fe chain on B-2D/Ag(111): electron charge density induced upon the adsorption of Fe chain, plotted in the chain plane (dashed black line) perpendicular to the substrate. The thermographic scale is in electrons/Bohr^3. For clarity reasons only Fe atoms, depicted by yellow spheres, are shown in the bottom panel.

electron density plot in Fig. 5 shows the redistribution of electrons upon the interaction of Fe wire with the B-2D/Ag(111). The plot in the plane of the chain, perpendicular to the substrate, reveals that the electronic orbitals of the closest Fe atoms directly overlap, at variance with the nearest neighbors at the distance of 3.36 Å whose interaction is mediated by two boron atoms rounded by light blue circles in the top panel of Fig. 5.

Four different spin configurations of the well-separated Fe chains grown above (A chains) or under (U chains) the borophene depicted in Fig. 6(a) are schematically presented in Fig. 6(b) and labeled as A_i and U_i, $i \in \{0, 1, 2, 3\}$, respectively. We assumed that energy differences of distinct configurations obtained from DFT calculations can be described with the Ising model

$$E_{\text{Ising}} = J_1(M_1M_2 + M_3M_4) + J_2(M_2M_3 + M_4M_1), \quad (1)$$

where the exchange interaction is limited to the nearest neighbors (NN). The J_1 and J_2 represent the exchange constants between the NN with two different interatomic distances, as depicted in Fig. 6(a). The M_i are magnetic moments at four different Fe sites inside the unit cell as determined from DFT calculations. It turns out that, for a given spin configuration, the absolute values of magnetic moments of all Fe atoms are the same. The DFT results of energies of different spin configurations, relative to the one with the lowest energy, as well as the absolute values of Fe magnetic moments, are presented in Table II. For both A and U chains the ferromagnetic configurations (A_0 nd U_0) are the most favorable. The plots in Figs. 6(c) and 6(d) show the perfect match between the DFT results and the Ising model for the exchange constants $J_1 = 17$ and $J_2 = 18$ meV, for A chain and $J_1 = 28$ and $J_2 = 18$ meV in the case of the U chains. From the plot in Figs. 6(c) and 6(d) it is noticeable that the spin configurations A_1 and A_2, which can be viewed as two different antifferomagnetic arrangements of ferromagnetically coupled dimers, are nearly degenerate. This degeneracy is lifted in the U chain, where the more pronounced dimerization affects the exchange interaction and results in different coupling constants between M_1 and M_2 from that between M_2 and M_3. It is worth noting that the

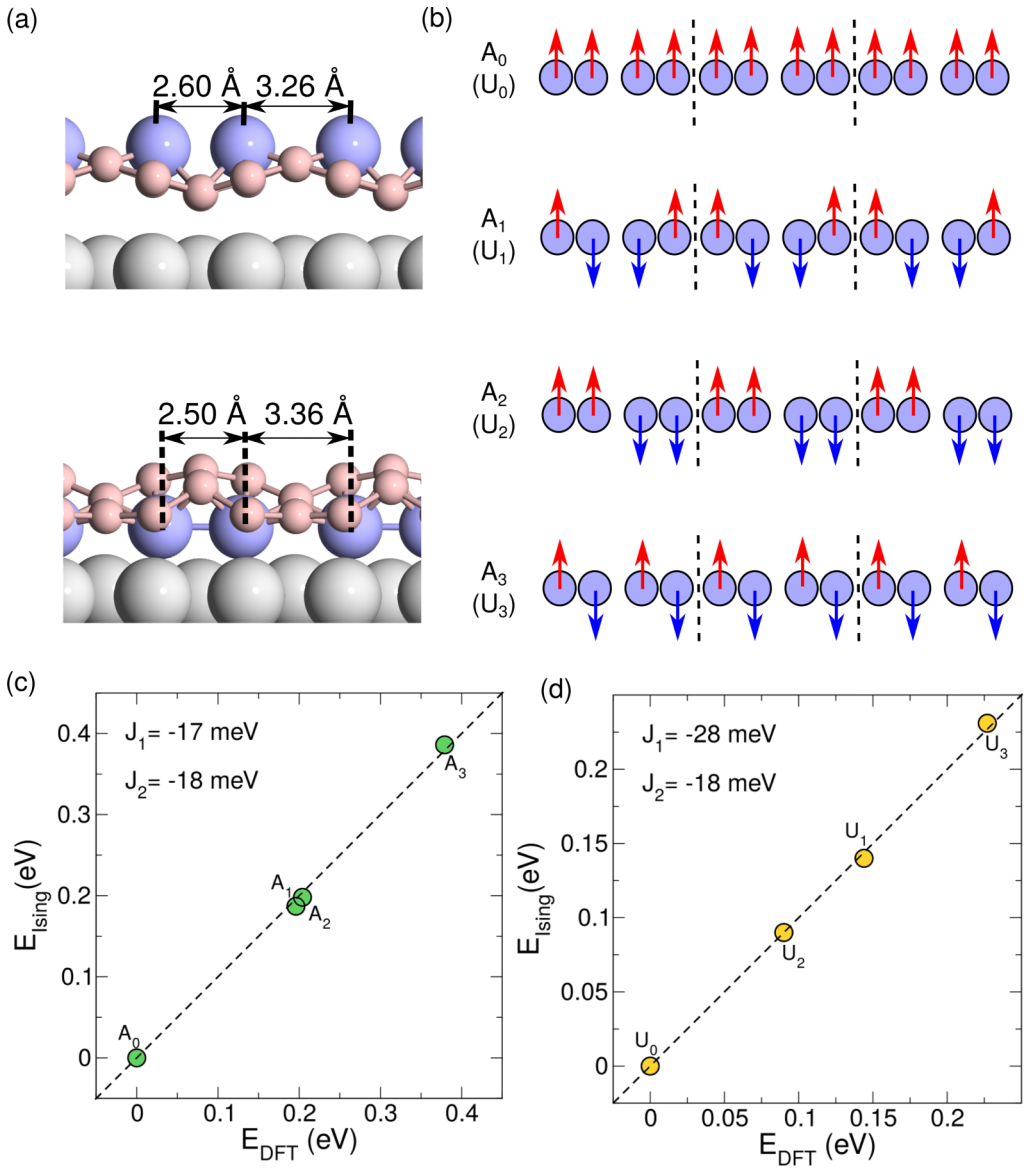

FIG. 6. (a) Side views of the Fe chains above (top panel) and under (lower panel) B-2D, supported by Ag(111); (b) schematic plot of four different spin configuration of Fe atoms in an infinite Fe chain at B-2D/Ag(111). The black dotted lines mark the unit cell along the chain axis, used in DFT calculations; correlation between DFT-calculated energy differences and the corresponding values of considered spin configurations obtained using the Ising model [Eq. (1)] for Fe chain (c) above (A) and (d) under (U) the B-2D sheet.

TABLE II. Relative energies of different spin configuration in Fig. 6(b), calculated using DFT (E_{DFT}), the corresponding values obtained from the Ising model (Eq. (1)), and the absolute values of the magnetic moments of Fe atoms.

Spin config.	E_{DFT} (eV)	E_{Ising} (eV)	Magnetic moment (μ_B/atom)
A_0	0.00	0.00	1.67
A_1	0.20	0.19	1.69
A_2	0.20	0.20	1.66
A_3	0.38	0.39	1.63
U_0	0.00	0.00	1.15
U_1	0.14	0.14	1.19
U_2	0.09	0.09	1.14
U_3	0.23	0.23	1.01

difference in the energy of ground magnetic state and the least favorable of studied configurations is largely reduced in the U chain owing to lower magnetic moments of Fe atoms as compared to A chain.

When Fe chains were close-packed [Fig. 4(b)], we also found a strong dimerization of the Fe atoms [Fig. 7(a)]. Furthermore, a small interwire distance of 5.07 Å causes a substantial interaction of the magnetic moments from neighboring chains. Thus, we considered close-packed chains as a 2*D* magnet and inspected eight different magnetic configurations, depicted in Fig. 7(b). Their energies, relative to the energy of the most favorable configuration, calculated using DFT, are presented in Table III. The B-2D corrugation is smaller than for well-separated chains and reaches the values of 1.03 and 1.04 Å for chains above and below the sheet. To fit DFT results to a 2*D* Ising model, in addition to the coupling

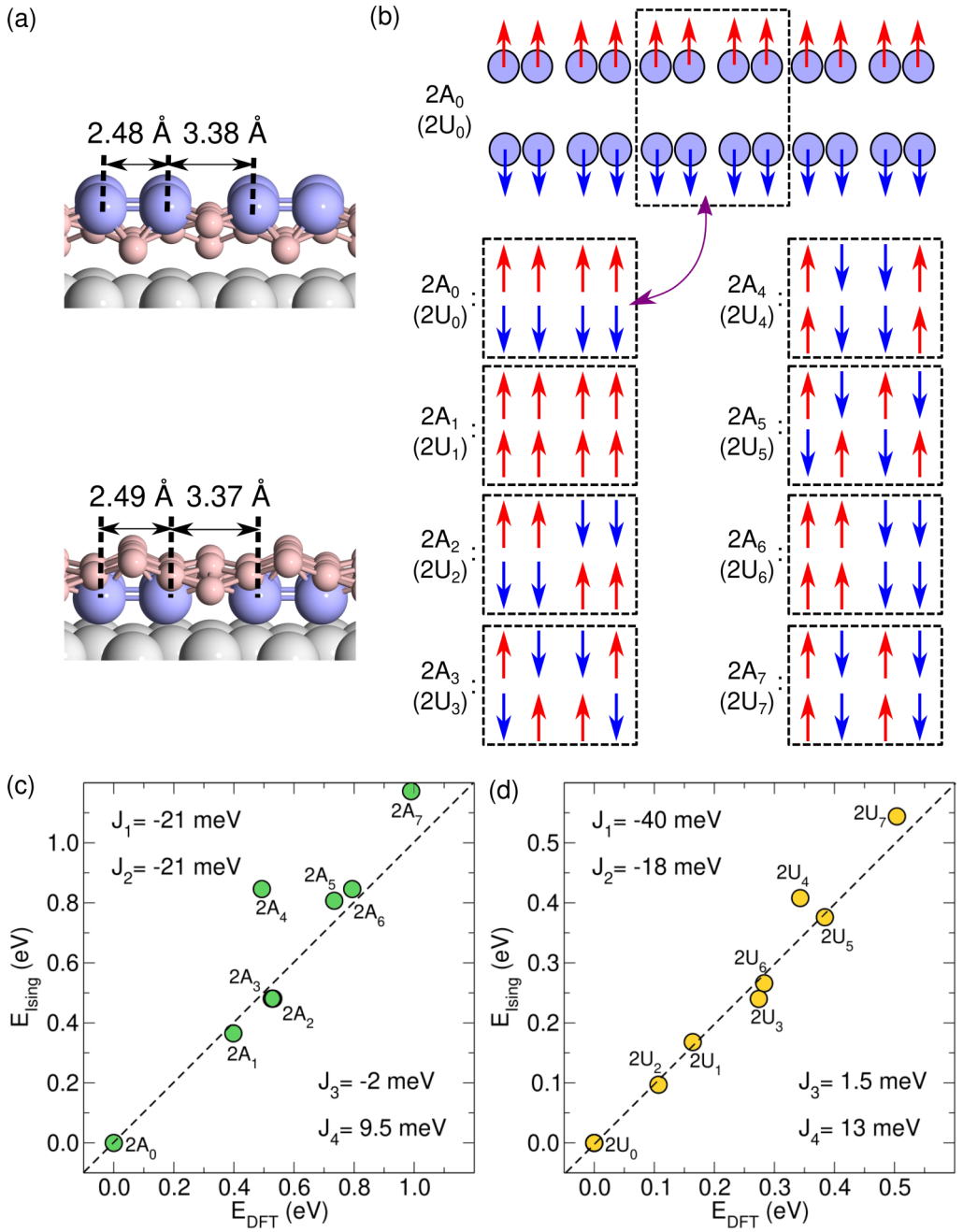

FIG. 7. (a) Side views of the close-packed Fe chains above (top panel) and under (lower panel) B-2D, supported by Ag(111); (b) schematic plot of unit cell (black rectangle) for eight different spin configuration of closely packed Fe chains at B-2D/Ag(111); correlation between DFT-calculated energy differences and the corresponding values of considered spin configurations obtained using Eq. (2) for Fe chains (c) above (A) and (d) under (U) the B-2D sheet.

constants used for the 1D model [Eq. (1)] we introduce the J_3 as a measure of the coupling between the next-nearest neighbors within the same chain, and the J_4, which accounts for the interaction between closest Fe atoms from neighboring chains [Fig. 4(b)]. Hence, the 2*D* Ising model reads

$$E_{\text{Ising}} = J_1(M_1M_2 + M_3M_4 + {}') + J_2(M_2M_3 + M_4M_1 + {}') + 2J_3(M_1M_3 + M_2M_4 + {}') + 2J_4\sum_{i=1}^{4} M_iM_{i'}, \tag{2}$$

where with $'$ we denote the terms analogous to the first two written in each bracket but counting atoms from the second chain in the unit cell. Similarly to well-separated chains, ferromagnetic ordering within the close-packed chains are the most favorable one. On the other hand, the interchain exchange interaction favors the antiferromagnetic coupling so that the spins in the most stable configurations on the neighboring chains are of opposite signs [$2A_0$ and $2U_0$ configurations in Fig. 7(b)]. As expected from the observed preferred intra- and interchain ordering, the least favorable magnetic configurations have completely opposite spin

TABLE III. Relative energies of different spin configurations in Fig. 7(b), calculated using DFT (E_{DFT}), the corresponding values obtained from the Ising model [Eq. (2)], and the absolute values of the magnetic moments of Fe atoms.

Spin config.	E_{DFT} (eV)	E_{Ising} (eV)	Magnetic moment (μ_B/atom)
$2A_0$	0.00	0.00	1.65
$2A_1$	0.40	0.37	1.54
$2A_2$	0.53	0.48	1.56
$2A_3$	0.53	0.48	1.62
$2A_4$	0.49	0.85	1.57
$2A_5$	0.73	0.81	1.47
$2A_6$	0.79	0.85	1.53
$2A_7$	0.99	1.17	1.47
$2U_0$	0.00	0.00	1.10
$2U_1$	0.16	0.17	0.82
$2U_2$	0.11	0.10	1.03
$2U_3$	0.27	0.24	0.99
$2U_4$	0.34	0.41	0.79
$2U_5$	0.38	0.38	0.72
$2U_6$	0.28	0.27	0.88
$2U_7$	0.50	0.54	0.09

ordering from the $2A_0$ and $2U_0$ configurations – antiferromagnetic coupling within the chain and ferromagnetic coupling between the chains [$2A_7$ and $2U_7$ in Fig. 7(b)]. In general, the plots presented in Figs. 7(c) and 7(d) show an excellent agreement between DFT results and the 2*D* Ising model, with the exception of a marked discrepancy regarding the configuration $2A_4$.

C. Monte Carlo simulations of critical temperatures

Standard DFT calculations can only predict magnetic properties at $T = 0$ K. The robustness of the long-range magnetic order, which sustains the thermal fluctuations up to critical temperature (T_C), must be explored using the alternative theoretical approaches. Therefore, assuming that Fe atoms at B-2D/Ag(111) represent a 2*D* lattice of classical spins, we employed Monte Carlo (MC) simulations to calculate the T_C of the structures with Fe atoms being adsorbed above (A) or under (U) the borophene supported by Ag(111). The exchange parameters used in the simulations are extracted from DFT calculations employing the procedure described in the text above, and their values are depicted in the Figs. 7(c) and 7(d). It turns out that calculated T_C greatly differ depending on the spin dimensionality, as demonstrated for CrI_3, where the Ising model overestimates the critical temperature by a factor of three when compared to the Heisenberg model and the values derived from measurements [50].

Firstly, assuming that the dynamics of the Fe-based magnet above and under the B-2D supported by Ag(111) can be described within the Ising model, we estimated T_C from the corresponding MC simulations. Figures 8(a) and 8(b) presents the temperature dependence of the sublattice magnetization for the 2*D* Ising model of Fe atoms at B-2D/Ag(111), for adatoms above and under the sheet, respectively. The T_C is

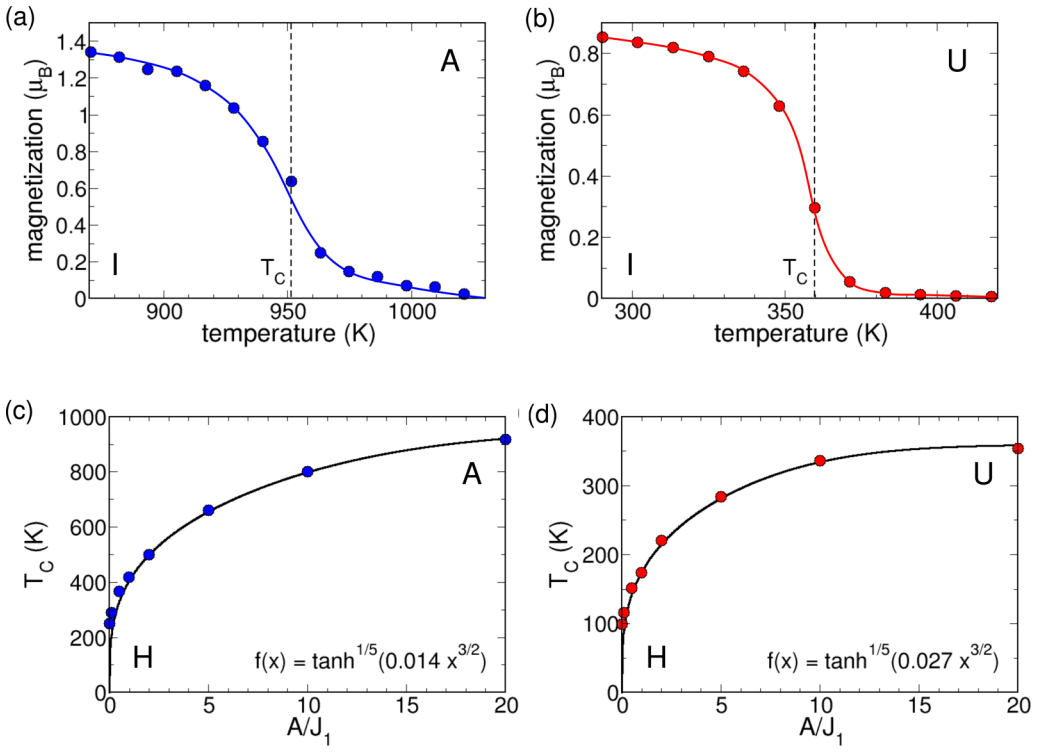

FIG. 8. Temperature dependence of the magnetization of Fe-based 2*D* magnets obtained from Monte Carlo simulations, considering Fe 2*D* structure (a) above (A) and (b) under (U) B-2D/Ag(111) and assuming that the magnetic properties can be described using the classical Ising (I) model. Critical temperature of the Fe-based 2*D* magnets (c) above (A) and (d) under (U) B-2D/Ag(111) as a function of scaled anisotropy A/J_1 calculated combining Monte Carlo simulations and the Heisenberg model with single-ion anisotropy.

determined as the temperature where the specific heat reaches maximum. The calculated T_C of the 2*D* magnet above B-2D/Ag(111) of 950 K is considerably higher when compared to the Fe 2*D* structure formed under borophene where we obtained the value of 360 K.

The next step in the MC simulations was to go beyond the Ising model. Preserving the same exchange interaction parameters as in the Ising model, we considered magnetic moments on Fe sites as classical 3D vectors for which we carried out the MC simulations in the framework of the Heisenberg model, adding to Eq. (2) the single-ion anisotropy (SIA) energy term

$$E_{\mathrm{SIA}} = A \sum_i \left(M_i^z\right)^2, \tag{3}$$

where the A represents the SIA parameter for Fe. The addition of the anisotropy term is essential for existance of the long-range order in 2*D* Heisenberg model at nonzero temperature [51–53]. Torelli and Olsen [54] demonstrated that T_C^{Ising} calculated from the Ising model slowly approaches the result obtained from the Heisenberg model with an added SIA term in the limit $A/J \to \infty$. Following the methodology described in Ref. [54] we performed MC simulations for the anisotropic Heisenberg model, considering several values of the A/J_1 parameter, as shown in Figs. 8(c) and 8(d). Results from MC simulations were then fitted to the analytical functions of the form

$$T_C = T_C^{\mathrm{Ising}} f(A/J_1), \tag{4}$$

with

$$\begin{aligned} f(x) &= \tanh^{1/5}(0.014\, x^{3/2}) \qquad (A-\text{magnet}), \\ f(x) &= \tanh^{1/5}(0.027\, x^{3/2}) \qquad (U-\text{magnet}), \end{aligned} \tag{5}$$

From new DFT calculations, which include spin-orbit interaction, we were able to estimate the A parameters for Fe, and found the values of -0.2 and -0.1 meV, for Fe atom within 2*D* magnets above and below the borophene sheet. We plug in these numbers into Eqs. (4) and (5) and we finally determined the T_C of 105 and 30 K, for the A and U-2D magnets, respectively. These results indicate that the studied structures cannot sustain the long-range magnetic order above 105 K, as estimated from the anisotropic Heisenberg model, and that the Ising model overestimates the T_C approximately by factor of 10.

IV. CONCLUSIONS

Combining DFT calculations and Monte Carlo simulations we studied magnetic nanostructures formed upon Fe adsorption at B-2D supported by Ag(111) surface. *Ab-initio* calculations revealed a strong preference for Fe adatoms to bind to the holes in B-2D thus filling the regular 2*D* hole pattern spreading over the sheet. All studied Fe nanostructures are more stable when metal atoms are intercalated between B-2D and Ag(111) surface than the structures with the adsorbates at the B-2D surface. Yet, due to considerable barrier for Fe diffusion through the holes, the metastable surface nanostructures could exist at low or modest temperatures. The ground state spin configuration of the 2*D* structure of Fe atoms exhibits antiferromagnetic coupling of closely packed ferromagnetic chains. From the magnetic moments of Fe atoms and energy differences between the ground state and spin configurations with higher energies, both quantities obtained using DFT, we were able to determine exchange constants between Fe atoms. The exchange constants were plugged into Monte Carlo simulations to calculate critical temperatures of Fe-based 2*D* magnets within the framework of the anisotropic Heisenberg model, where the values of 105 and 30 K were found, for Fe-2D structures above and under B-2D supported by Ag(111), respectively. These results indicate that further improvements are required for the applications in technologies operating at room temperature. A possible route to increase the T_C is to replace Fe with Co atoms, since it is known that Co nanostructures at crystalline surfaces carry out rather high magnetic anisotropy energy [55].

ACKNOWLEDGMENTS

We thank M. Peressi for a fruitful discussion, and acknowledge PRACE for awarding us access to the Beskow supercomputer hosted by the PDC Centre for High Performance Computing, KTH Royal Institute of Technology and CINECA for the computational resources obtained through the ISCRA initiative and the agreement with the University of Trieste. We also acknowledge the financial support from the Italian Ministry of Foreign Affairs and International Cooperation (Executive Programme with Serbia 2019-2021 - "Progetti di Grande Rilevanza").

[1] K. S. Novoselov, A. K. Geim, S. V. Morozov, D. Jiang, M. I. Katsnelson, I. V. Grigorieva, S. V. Dubonos, and A. A. Firsov, Nature (London) **438**, 197 (2005).
[2] K. S. Novoselov, A. K. Geim, S. V. Morozov, D. Jiang, Y. Zhang, S. V. Dubonos, I. V. Grigorieva, and A. A. Firsov, Science **306**, 666 (2004).
[3] A. K. Geim and K. S. Novoselov, Nat. Mater. **6**, 183 (2007).
[4] S. Z. Butler, S. M. Hollen, L. Y. Cao, Y. Cui, J. A. Gupta, H. R. Gutierrez, T. F. Heinz, S. S. Hong, J. X. Huang, A. F. Ismach *et al.*, ACS Nano **7**, 2898 (2013).
[5] S. Lebegue and O. Eriksson, Phys. Rev. B **79**, 115409 (2009).
[6] H. Sahin, S. Cahangirov, M. Topsakal, E. Bekaroglu, E. Akturk, R. T. Senger, and S. Ciraci, Phys. Rev. B **80**, 155453 (2009).
[7] F. A. Rasmussen and K. S. Thygesen, J. Phys. Chem. C **119**, 13169 (2015).
[8] J.-G. Park, J. Phys.: Condens. Matter **28**, 301001 (2018).
[9] C. Gong and X. Zhang, Science **363**, 706 (2019).
[10] B. Huang, G. Clark, E. Navarro-Moratalla, D. R. Klein, R. Cheng, K. L. Seyler, D. Zhong, E. Schmidgall, M. A. McGuire, D. H. Cobden *et al.*, Nature (London) **546**, 270 (2017).
[11] J.-U. Lee, S. Lee, J. H. Ryoo, S. Kang, T. Y. Kim, P. Kim, C.-H. Park, J.-G. Park, and H. Cheong, Nano Lett. **16**, 7433 (2016).

[12] C. Gong, L. Li, Z. Li, H. Ji, A. Stern, Y. Xia, T. Cao, W. Bao, C. Wang, Y. Wang *et al.*, Nature **546**, 265 (2017).
[13] O. V. Yazyev and L. Helm, Phys. Rev. B **75**, 125408 (2007).
[14] R. R. Nair, M. Sepioni, I.-L. Tsai, O. Lehtinen, J. Keinonen, A. V. Krasheninnikov, T. Thomson, A. K. Geim, and I. V. Grigorieva, Nat. Phys. **8**, 199 (2012).
[15] L. Ćirić, D. M. Djokić, J. Jaćimović, A. Sienkiewicz, A. Magrez, L. Forró, Ž. Šljivančanin, M. Lotya, J. N. Coleman, Phys. Rev. B **85**, 205437 (2012).
[16] Y. Son, M. Cohen, S. Louie, S, Nature (London) **444**, 347 (2006).
[17] M. Slota, A. Keerthi, W. K. Myers, E. Tretyakov, M. Baumgarten, A. Ardavan, H. Sadeghi, C. J. Lambert, A. Narita, K. Müllen *et al.*, Nature (London) **557**, 691 (2018).
[18] H. González-Herrero, J. M. Gómez-Rodríguez, P. Mallet, M. Moaied, J. J. Palacios, C. Salgado, M. M. Ugeda, J.-Y. Veuillen, F. Yndurain, and I. Brihuega, Science **352**, 437 (2016).
[19] Ž. Šljivančanin, R. Balog, L. Hornekær, Chem. Phys. Lett. **541**, 70 (2012).
[20] T. L. Makarova, A. L. Shelankov, A. A. Zyrianova, A. I. Veinger, T. V. Tisnek, E. Laehderanta, A. I. Shames, A. V. Okotrub, L. G. Bulusheva, G. N. Chekhova *et al.*, Sci. Rep. **5**, 13382 (2015).
[21] K. Zhang, S. Feng, J. Wang, A. Azcatl, N. Lu, R. Addou, N. Wang, C. Zhou, J. Lerach, V. Bojan *et al.*, Nano. Lett. **15**, 6586 (2015).
[22] V. Kochat, A. Apte, J. A. Hachtel, H. Kumazoe, A. Krishnamoorthy, S. Susarla, J. C. Idrobo, F. Shimojo, P. Vashishta, R. Kalia *et al.*, Adv. Mater. **29**, 1703754 (2017).
[23] S. Stavrić, M. Belić, Ž. Šljivančanin, Carbon **96**, 216 (2016).
[24] D. N. Sredojević, M. R. Belić, and Ž. Šljivančanin, J. Phys. Chem. C **124**, 16860 (2020).
[25] B. J. Feng, J. Zhang, R. Y. Liu, T. Iimori, C. Lian, H. Li, L. Chen, K. Wu, S. Meng, F. Komori, and I. Matsuda, Phys. Rev. B **94**, 041408(R) (2016).
[26] A. J. Mannix, X. F. Zhou, B. Kiraly, J. D. Wood, D. Alducin, B. D. Myers, X. L. Liu, B. L. Fisher, U. Santiago, J. R. Guest *et al.*, Science **350**, 1513 (2015).
[27] Z. H. Zhang, Y. Yang, G. Y. Gao, and B. I. Yakobson, Angew. Chem., Int. Ed. **54**, 13022 (2015).
[28] Z. Zhang, A. J. Mannix, X. L. Liu, Z. Hu, N. P. Guisinger, M. C. Hersam, and B. Y. Yakobson, Sci. Adv. **5**, eaax0246 (2019).
[29] W. B. Li, L. J. Kong, C. Y. Chen, J. Gou, S. X. Sheng, W. F. Zhang, H. Li, L. Chen, P. Cheng, and K. H. Wu, Sci. Bull. **63**, 282 (2018).
[30] B. Kiraly, X. L. Liu, L. Q. Wang, Z. H. Zhang, A. J. Mannix, B. L. Fisher, B. I. Yakobson, M. C. Hersam, and N. P. Guisinger, ACS Nano **13**, 3816 (2019).
[31] R. T. Wu, I. K. Drozdov, S. Eltinge, P. Zahl, S. Ismail-Beigi, I. Božović, and A. Gozar, Nat. Nanotech. **14**, 44 (2019).
[32] Y. Wang, Y. Park, L. Qiu, I. Mitchell, and F. Ding, J. Phys. Chem. Lett. **11**, 6235 (2020).
[33] M. Gao, Q.-Z. Li, X.-W. Yan, and J. Wang, Phys. Rev. B **95**, 024505 (2017).
[34] C. Hou, G. Tai, Z. Wu, and J. Hao, ChemPlusChem **85**, 2186 (2020).
[35] A. Mannix, B. Kiraly, M. C. Hersam, and N. P. Guisinger, Nat. Rev. Chem. **1**, 0014 (2017).
[36] P. Giannozzi, S. Baroni, N. Bonini, M. Calandra, R. Car, C. Cavazzoni, D. Ceresoli, G. L. Chiarotti, M. Cococcioni, I. Dabo *et al.*, J. Phys.: Condens. Matter **21**, 395502 (2009).
[37] P. Giannozzi, O. Andreussi, T. Brumme, O. Bunau, M. B. Nardelli, M. Calandra, R. Car, C. Cavazzoni, D. Ceresoli, M. Cococcioni *et al.*, J. Phys.: Condens. Matter **29**, 465901 (2017).
[38] J. P. Perdew, K. Burke, and M. Ernzerhof, Phys. Rev. Lett. **77**, 3865 (1996).
[39] D. C. Liu and J. Nocedal, Math. Program. **45**, 503 (1989).
[40] H. J. Monkhorst and J. D. Pack, Phys. Rev. B **13**, 5188 (1976).
[41] P. Blaha, K. Schwarz, F. Tran, R. Laskowski, G. Madsen, and L. Marks, J. Chem. Phys. **152**, 074101 (2020).
[42] G. H. O. Daalderop, P. J. Kelly, and M. F. H. Schuurmans, Phys. Rev. B **41**, 11919 (1990).
[43] S. R. Bahn and K. W. Jacobsen, Comput. Sci. Eng. **4**, 56 (2002).
[44] A. H. Larsen, J. J. Mortensen, J. Blomqvist, I. E. Castelli, R. Christensen, M. Dułak, J. Friis, M. N. Groves, B. Hammer, C. Hargus *et al.*, J. Phys.: Condens. Matter **29**, 273002 (2017).
[45] A. Kokalj, J. Mol. Graphics Modell. **17**, 176 (1999).
[46] X. Wu, J. Dai, Y. Zhao, Z. Zhou, J. Yang, and X. C. Zeng, ACS Nano **6**, 7443 (2012).
[47] Q. Zhong, J. Zhang, P. Cheng, B. Feng, W. Li, S. Sheng, H. Li, S. Meng, L. Chen, and K. Wu, J. Phys.: Condens. Matter **29**, 095002 (2017).
[48] S. Sheng, J.-B. Wu, X. Cong, Q. Zhong, W. Li, W. Hu, J. Gou, P. Cheng, P.-H. Tan, L. Chen *et al.*, ACS Nano **13**, 4133 (2019).
[49] G. L. Gutsev and C. W. Bauschlicher, J. Phys. Chem. A **107**, 7013 (2003).
[50] D. Torelli, K. S. Thygesen, and T. Olsen, 2D Mater. **6**, 045018 (2019).
[51] N. D. Mermin and H. Wagner, Phys. Rev. Lett. **17**, 1133 (1966).
[52] K. S. Burch, D. Mandrus, and J.-G. Park, Nature (London) **563**, 47 (2018).
[53] C. S. Xu, J. S. Feng, H. J. Xiang, and L. Bellaiche, npj Comput. Mater. **4**, 57 (2018).
[54] D. Torelli and T. Olsen, 2D Mater. **6**, 015028 (2019).
[55] P. Gambardella, S. Rusponi, M. Veronese, S. S. Dhesi, C. Grazioli, A. Dallmeyer, I. Cabria, R. Zeller, P. H. Dederichs, K. Kern *et al.*, Science **300**, 1130 (2003).